

EZO A - A catalogue of EBHIS H I detected galaxies in the northern Zone of Avoidance

A.C. Schröder,^{1*} L. Flöer,² B. Winkel² and J. Kerp²

¹South African Astronomical Observatory, PO Box 9, Observatory 7935, Cape Town, South Africa

²Argelander Institut für Astronomie, Auf dem Hügel 71, 53121 Bonn, Germany

Accepted XXX. Received YYY; in original form ZZZ

ABSTRACT

We present a catalogue of galaxies in the northern Zone of Avoidance (ZoA), extracted from the shallow version of the blind H I survey with the Effelsberg 100 m radio telescope, EBHIS, that has a sensitivity of 23 mJy beam⁻¹ at 10.24 km s⁻¹ velocity resolution. The catalogue comprises 170 detections in the region $\delta \geq -5^\circ$ and $|b| < 6^\circ$. About a third of the detections ($N = 67$) have not been previously recorded in H I. While 29 detections have no discernible counterpart at any wavelength other than H I, 48 detections (28%) have a counterpart visible on optical or NIR images but are not recorded as such in the literature. New H I detections were found as close as 7.5 Mpc (EZO A J2120+45), and at the edge of the Local Volume, at 10.1 Mpc, we have found two previously unknown dwarf galaxies (EZO A J0506+31 and EZO A J0301+56). Existing large-scale structures crossing the northern ZoA have been established more firmly by the new detections, with the possibility of new filaments. We conclude that the high rate of 39% new H I detections in the northern ZoA, which has been extensively surveyed with targeted observations in the past, proves the power of blind H I surveys. The full EBHIS survey, which will cover the full northern sky with a sensitivity comparable to the HIPASS survey of the southern sky, is expected to add many new detections and uncover new structures in the northern ZoA.

Key words: galaxies: distances and redshifts – galaxies: fundamental parameters – large-scale structure of the universe – surveys – radio lines: galaxies

1 INTRODUCTION

Surveys of the sky at the 21 cm wavelength emission of the neutral hydrogen (H I) are a useful means to probe evenly for gas-rich galaxies in the local universe, including galaxies behind the Galactic plane where dust and high stellar densities prevent optical surveys from obtaining a full census of galaxies in a magnitude- or diameter-limited sample. H I selected galaxy samples are thus free from biases due to imperfect corrections for Galactic foreground extinctions (e.g., Riad, Kraan-Korteweg & Woudt 2010) and stellar densities (e.g., Schröder, van Driel & Kraan-Korteweg 2019).

Most H I surveys are pointed observations of a sample of galaxies, usually selected in the optical or near-infrared (NIR). Systematic blind surveys, that is, the scanning of the sky to find extragalactic H I emission independent of prior positional knowledge, became only practicable with the event of multibeam receivers but are still very time consuming.

The southern sky has been extensively surveyed in H I

using the 64 m Parkes radio telescope (PKS). The blind survey HIPASS covers all of the southern sky and part of the northern sky up to $\delta = +25^\circ$ (Meyer et al. 2004; Wong et al. 2006) with a sensitivity of ~ 13 mJy beam⁻¹ (at 18 km s⁻¹ velocity resolution). In addition, the Galactic plane, also called Zone of Avoidance (ZoA) in extragalactic studies, was surveyed more deeply with a sensitivity of ~ 6 mJy beam⁻¹ at 27 km s⁻¹ velocity resolution (HIZOA; Staveley-Smith et al. 2016; Donley et al. 2005).

There are no equivalent all-sky surveys of the northern sky. The regions accessible by the 305 m Arecibo telescope are covered by ALFALFA (Haynes, Giovanelli et al. 2018) and the still on-going ALFA ZoA (McIntyre et al. 2015; Henning et al. 2008) with a velocity resolution of 9 km s⁻¹ and a sensitivity of 2 mJy beam⁻¹ and 1 mJy beam⁻¹, respectively. Further north exists the HIJASS survey (Lang et al. 2003) conducted with the 76 m Lovell telescope at Jodrell Bank with a published catalogue covering selected parts of the northern sky at varying sensitivity (13–16 mJy beam⁻¹, 18 km s⁻¹ velocity resolution). The northern ZoA was partly surveyed by the 25 m Dwingeloo

* E-mail: anja@saao.ac.za

Table 1. EBHIS survey parameters

Parameter	Value
Coverage	$\delta \geq -5^\circ$
Velocity range	$-600 \text{ km s}^{-1} < cz < 18,000 \text{ km s}^{-1}$
Velocity resolution	10.24 km s^{-1}
Beam size (FWHP)	10'8
Integration time	$\sim 35 \text{ s beam}^{-1}$
Cube rms	23 mJy beam^{-1}

telescope at a sensitivity of 40 mJy beam^{-1} (Henning et al. 1998; Rivers, Henning & Kraan-Korteweg 1999).

The Effelsberg–Bonn H I Survey (EBHIS, Kerp et al. 2011, Winkel et al. 2010), an all-sky survey conducted with the 100 m Effelsberg radio telescope, will fill this gap and cover the full northern sky homogeneously ($\delta \geq -5^\circ$) with an ultimate sensitivity of 16 mJy , comparable to HIPASS. We present here results from the shallow survey at a sensitivity of 23 mJy beam^{-1} (Flöer, Winkel & Kerp 2014) at a velocity resolution of 10 km s^{-1} and covering the northern ZoA ($|b| < 6^\circ$).

A number of H I surveys are imminent, using the upcoming SKA precursors, e.g., ASKAP (Johnston et al. 2008) in the south and APERTIF (Oosterloo, Verheijen & van Cappellen 2010) and FAST (Li, Nan & Pan 2013; Nan et al. 2011) in the north; they will cover the sky to much higher sensitivities, but, as before, only the southern sky will be homogeneously and continuously covered by ASKAP’s all-sky H I survey WALLABY (Koribalski 2012; Duffy et al. 2012), whereas the northern sky will only be surveyed in part, shared between APERTIF and FAST. Hence, EBHIS will continue to be the only homogeneous northern sky blind H I survey for quite some time to come.

This paper is organised as follows. Section 2 explains the observations and data reduction; Sec. 3 presents the catalogue and Sec. 4 the cross-matched data at other wavelengths. The completeness and reliability of the catalogue is discussed in Sec. 5 and the H I properties of the sample in Sec. 6. How the newly found galaxies fit in with the large scale structures in the local universe is analysed in Sec. 7. Section 8 gives a summary. The catalogue, the cross-match table and the H I profiles are available online.

2 OBSERVATIONS AND DATA REDUCTION

EBHIS (Kerp et al. 2011) is a blind H I survey of the sky north of $\delta = -5^\circ$, conducted with the Effelsberg 100 m radio telescope. The Galactic part of the survey ($-600 \leq v_{\text{lsr}} \leq 600 \text{ km s}^{-1}$) has been published by Winkel et al. (2016). The here presented catalogue is based on pre-release H I data from the first of two runs, which was finished in April 2013. The second run is on-going and will improve the sensitivity of EBHIS by about 30%. The observational parameters of the shallow survey are summarised in Table 1.

A detailed description of the data reduction techniques applied is given in Winkel et al. (2016); in summary these are: (1) raw data spectra were processed manually and automatically to search for radio frequency interference (RFI); (2) a frequency-dependent bandpass (gain) correc-

tion was applied; (3) flux-density or brightness-temperature calibration was based on the standard IAU source S7 (Kalberla, Mebold & Reif 1982); (4) baselines were subtracted via a 2D polynomial fitting routine; (5) the side-lobe contribution (so-called stray radiation) was removed; (6) the resulting, calibrated spectra were gridded into data cubes.

For the extragalactic part of the data, mostly the same recipe and software was applied, with two noteworthy differences. First, stray-radiation removal was not necessary and, second, the baseline subtraction was done differently. The 2D polynomial fits to the baseline that were used for the Galactic part were not practical for the extragalactic data, since a fit to the full velocity range of $-600 \leq v_{\text{lsr}} \leq 18,000 \text{ km s}^{-1}$ would require a much higher order polynomial. A possible solution was to fit chunks of data at a time, that is, about 1000 spectral channels interleaved by 500 channels. This was found to be relatively time consuming, but yielded results that are comparable to the Galactic EBHIS data quality. However, with a median spectrum computed over a larger field (e.g., $10^\circ \times 10^\circ$), small-scale residual ripples may appear in the baseline.

It was therefore decided to follow a slightly different approach for the extragalactic baseline removal. Before any polynomial fitting was performed, a median spectrum of the raw calibrated spectra was calculated for each subscan, feed and polarisation channel which was then subtracted from each individual spectrum. This effectively removed the small-scale ripples. For the Galactic velocity interval such an approach would not have been possible because the H I line is present in every single spectrum. For the extragalactic part, however, only a very small fraction of the data contains H I line signals and sufficient “baseline”, surrounding the sources of interest, is available. Since continuum sources usually have an impact on the baseline shape (see, e.g., Winkel et al. 2016), spectra such affected were neglected for the median-calculation. As also explained by Winkel et al. (2016), the baselines have a noticeable time-dependency. Therefore, an additional low-order 2D polynomial fit was performed and subtracted to account for the temporal evolution.

Finally, to ease working with the spectra, data cubes of size $12^\circ \times 12^\circ$ (with an overlap of $\Delta\ell = 1^\circ$ on each side) are produced and spectrally binned with a factor of eight, leading to an effective spectral resolution of 10.24 km s^{-1} , to reduce the data volume.

3 SAMPLE COMPILATION AND H I PARAMETERISATION

For the search in the ZoA, cubes with a velocity range of $-500 \leq cz \leq 12,500 \text{ km s}^{-1}$ and $12^\circ \times 12^\circ$ were produced with a spatial overlap of 1° in Galactic longitude. We adopted an upper velocity limit since we do not expect detections much above $10,000 \text{ km s}^{-1}$ at this sensitivity. The velocity axis in the cubes were converted from LSRK (kinematic local standard of rest) to v_{hel} (Kerr & Lynden-Bell 1986), and the intensity scale from Kelvin to Jansky. To ease the problem of strong baseline variations caused by continuum sources, we worked with two sets of cubes: the ‘normal’ ones, as are, and a set where a spline-based baseline was subtracted along each line of sight to remove the strongest baseline variations. This, however, caused troughs around

the brighter HI sources which may affect their visibility to the eye.

Each ZoA cube in both sets was visually inspected using the visualisation package KARMA (Gooch 1996). A comparison of the ensuing source lists from the two sets showed that, as expected, bright detections affected the baseline-splinefit and were often harder to see in the baseline-subtracted cubes, but the latter made it easier to find galaxies where strong baseline ripples occur. The resulting, comprehensive source list was re-checked and quality flags applied (based on signal-to-noise ratio, presence of baseline wiggles and visual appearance of the detection). Only detections deemed reliable were retained for the catalogue where those with a signal-to-noise ratio below 6 are considered marginal. Reliability determinations were based on independent judgements for two slices (XZ and ZY¹) of each set of cubes (using the appearance in the image and the individual line-of-sight profiles) as well as the final fitted profile; where in doubt we compared detections of similar quality to ensure homogeneity in the judgements. Detections which did not make this cut (e.g., with a too low signal-to-noise ratio or not convincingly real) were retained for comparison with the upcoming full EBHIS survey.

HI parameters were determined using the programme MBSPECT within the MIRIAD package (Sault, Teuben & Wright 1995). Zeroth moment maps were made for each detection using the non-baseline subtracted cubes, and positions were determined using a Gaussian fit. A one-dimensional Hanning-smoothed spectral profile was obtained by calculating the weighted sum of the emission at the resulting position. The spectrum was visually inspected and a low-order polynomial was fitted to the emission-free channels and subtracted. An integration over the channels containing the HI emission of the baseline-subtracted spectrum resulted in the total flux. The heliocentric velocity was taken to be the mean of the velocity values at the 50% mark of the peak flux density of the profile. Line widths at both the 50% as well as the 20% level of the peak flux density were determined using a width-maximising algorithm.

Errors were calculated using the formalism presented in Koribalski et al. (2004). The errors on velocities and line widths depend, among others, on the steepness of the profile edges and thus on the line width at 20% of peak flux density; in case this value could not be determined (where the signal was too close to the noise level, $N = 38$ profiles), we used the median steepness derived from our sample, ($w_{20} - w_{50}$) = 24.5 km s⁻¹, to calculate the errors for w_{50} and v_{hel} .

We have detected 170 HI sources. The catalogue and the HI profile plots are available online; Table 2 and Fig. 1 give the first 12 detections and profiles, respectively, as an example. On each profile, the peak as well as the 50% and 20% levels are noted with dots. Vertical lines indicate the spectral ranges used for baseline subtraction, and the linear or polynomial fit is shown. Table 2 lists HI parameters and derived quantities for the galaxies in the following columns:

Columns (1): Source name.

Columns (2a and 2b): Equatorial coordinates (J2000.0) of the fitted position.

Columns (3a and 3b): Galactic coordinates.

Column (4): Reddening $E(B - V)$ as derived from the IRAS/DIRBE maps (Schlegel, Finkbeiner & Davis 1998) and corrected with a factor of 0.86 as derived by Schlafly & Finkbeiner (2011).

Column (5): Heliocentric velocity and error, in km s⁻¹.

Column (6): Velocity width at 50% of peak flux density and associated error, in km s⁻¹.

Column (7): Velocity width at 20% of peak flux density and associated error, in km s⁻¹.

Column (8): HI flux integral and associated error, in Jy km s⁻¹.

Column (9): Signal-to-noise ration SNR using the peak flux.

Column (10): Velocity of the galaxy, in km s⁻¹, corrected to the Local Group frame of reference via:

$$v_{\text{LG}} = v_{\text{hel}} + 300 \sin \ell \cos b$$

Column (11): Distance to the galaxy in Megaparsec, based on v_{LG} and $H_0 = 75 \text{ km s}^{-1} \text{ Mpc}^{-1}$.

Column (12): Logarithm of the HI mass.

4 MULTIWAVELENGTH COUNTERPARTS

The search for counterparts (i.e., at wavelengths other than HI) was done using the following online literature databases and optical and NIR images: The NASA/IPAC Extragalactic Database (NED)², SIMBAD³, the SuperCOSMOS Sky Surveys⁴ (B -band), the Digitized Sky Surveys (DSS)⁵ (R - and I -band), 2MASS⁶ (K_s -band), UKIDSS⁷ and VISTA⁸ (both preferably K_s -band). The search procedure is described in detail in Staveley-Smith et al. (2016) with the main difference that the search radius (which depends on the spatial resolution of the HI data) was set to 3'.0.

The most likely counterpart was identified based on the HI parameters, the appearance of the galaxy on the images and the extinction information: Line widths were compared with the inclination and morphological type of the galaxies; the HI flux was compared with apparent brightness, size and optical velocity measurements (where available), taking into account the obscuring effect of the local extinction. Table 3 lists 16 detections and their counterparts (where available) as an example, the rest is available online only. There are three sub-sections: Table 3a gives the EZOA detections with either a single or no counterpart. Table 3b lists detections where more than one galaxy is assumed to contribute to the HI profile (note that in the case of EZOA J0440+49A and EZOA J0440+49B the profiles are confused but the detections could be fitted separately – they are thus listed in Table 3a). Table 3c presents those cases where more than one candidate was found but, judged by the profile, only

² <http://ned.ipac.caltech.edu>

³ <http://simbad.u-strasbg.fr/simbad/>

⁴ <http://www-wfau.roe.ac.uk/sss/>

⁵ <http://www3.cadc-ccda.hia-ihp.nrc-cnrc.gc.ca/en/dss/>

⁶ <http://irsa.ipac.caltech.edu/applications/2MASS/>

⁷ <http://surveys.roe.ac.uk/wsa/>

⁸ <http://horus.roe.ac.uk/vsa/>

¹ In the HI data cubes, X and Y are the two coordinates and Z is the velocity axis.

one of them is the likely counterpart. The columns are as follows:

Column (1): Source name as in Table 2.

Columns (2a and 2b): Galactic coordinates of the H I detection.

Column (3): Distance to the H I galaxy in Megaparsec, as in Table 2.

Column (4): Logarithm of the H I mass, as in Table 2.

Column (5): Extinction in the B -band, converted from $E(B - V)$ given in Table 2 using $R_B = 4.14$. A star denotes an extinction value deemed to be uncertain during the search (e.g., due to high spatial variability), whereas a question mark indicates the possibility that the extinction value might be erroneous.

Column (6): Classification of the counterpart; ‘d’ = definite, ‘p’ = probable, ‘a’ = ambiguous, ‘c’ = confused candidate; ‘-’ = no candidate.

Column (7): Flags for counterparts in major catalogues: ‘I’ stands for IRAS Point Source Catalog (Helou & Walker 1988), ‘M’ for 2MASX (Jarrett et al. 2000), ‘H’ for the HIPASS catalogues (South, Meyer et al. 2004 and North, Wong et al. 2006), ‘J’ for the HI Jodrell All Sky Survey (HI-JASS; Lang et al. 2003), ‘S’ for the H I Parkes ZOA Shallow Survey (HIZSS, Henning et al. 2000), and ‘Z’ for HI-ZOA publications (Juraszek et al. 2000; Donley et al. 2005; Staveley-Smith et al. 2016).

Column (8): Type of velocity measurement in the literature (from NED or HyperLEDA⁹): ‘o’ = optical, ‘h’ = H I.

Column (9): Source ‘l’ for coordinates from the literature: ‘N’ is listed in NED, ‘S’ is listed in SIMBAD. The flag ‘c’ stands for coordinates measured on DSS or NIR images (note that some published coordinates were not centred properly so we give the measured ones).

Column (10): Note in the appendix.

Columns (11a and 11b): Equatorial coordinates (J2000.0) of the counterpart.

Column (12): Distance between the H I fitted position and the counterpart position in arcminutes.

Column (13): One name in the literature of an optical- or NIR-known counterpart, in this order of preference: NGC, IC, UGC, ESO, CGMW, WEIN, 2MASS, others.

⁹ <http://leda.univ-lyon1.fr/>

Table 2: EZOA HI detections with measured and derived parameters

EZO A ID	RA	Dec	l	b	$E(B-V)$	v_{hel}	w_{50}	w_{20}	Flux	SNR	v_{LG}	D	$\log M_{\text{HI}}$
(1)	J2000.0 (2a)	(2b)	[deg] (3a)	[deg] (3b)	(4)	[km s^{-1}] (5)	[km s^{-1}] (6)	[km s^{-1}] (7)	[Jy km s^{-1}] (8)	(9)	[km s^{-1}] (10)	[Mpc] (11)	[M_{\odot}] (12)
J1825-0118	25 01.7	-01 30 13	28.57	5.18	1.38	2867± 7	347±13	...	27.2± 4.3	7.3	3010	40.1	10.01
J1853+0918	53 52.2	+09 49 41	41.97	3.93	0.79	4711± 7	283±13	336±20	12.4± 1.8	10.7	4911	65.5	10.10
J1856-0318	56 03.1	-03 14 28	30.57	-2.50	1.20	1585± 5	196±10	212±15	14.5± 2.9	7.6	1737	23.2	9.26
J1901+0619	01 34.4	+06 51 48	40.19	0.88	4.72	2945± 2	78± 4	105± 6	17.0± 1.5	24.2	3139	41.8	9.85
J1901-0419	01 46.2	-04 29 27	30.10	-4.34	0.68	1521± 5	131±11	159±16	13.2± 2.3	9.6	1671	22.3	9.19
J1910+0019	10 22.7	+00 31 05	35.56	-3.98	0.59	1498± 4	191± 8	204±12	11.3± 2.2	8.4	1672	22.3	9.12
J1912+1319	12 42.2	+13 24 28	47.26	1.46	2.51	2772± 5	114±10	136±15	8.2± 1.7	9.1	2992	39.9	9.49
J1915+1019	15 00.5	+10 16 53	44.76	-0.49	10.56	655± 1	77± 3	98± 4	20.3± 1.3	31.7	866	11.5	8.80
J1919+1419	19 53.2	+14 09 02	48.73	0.27	7.09	2811± 9	150±17	193±26	16.8± 3.6	7.3	3036	40.5	9.81
J1921+1419	21 38.8	+14 53 08	49.58	0.23	4.70	4075±11	75±21	123±32	7.1± 2.4	6.2	4303	57.4	9.74
J1921+0819	21 54.2	+08 18 55	43.81	-2.91	0.90	3082±11	115±22	164±33	5.2± 1.5	6.2	3289	43.9	9.37
J1922+1819	22 47.3	+18 45 13	53.12	1.82	2.81	3919± 4	329± 8	347±12	17.2± 2.1	10.2	4159	55.5	10.10
...													

Table 3: Crossmatches of the EZOA HI detections

EZO A ID	l	b	D	$\log M_{\text{HI}}$	A_B	class	IMHSZ	oh	lc	Note	RA	Dec	d_{sep}	Name
(1)	[deg] (2a)	[deg] (2b)	[Mpc] (3)	[M_{\odot}] (4)	[mag] (5)	(6)	(7)	(8)	(9)	(10)	J2000.0 (11a)	(11b)	[$^{\circ}$] (12)	(13)
(a) HI detections with single cross-matches:														
J1825-01	28.57	5.18	40.1	10.01	5.7	d	--H-Z	-h	-c	-	18 25 00.1	-01 28 33	1.6	...
J1853+09	41.97	3.93	65.5	10.10	3.3	d	-MH-Z	-h	Nc	-	18 53 47.5	09 51 14	2.0	2MASX J18534771+0951131
J1856-03	30.57	-2.50	23.2	9.26	5.0	-	--HSZ	-h	--	n
J1901+06	40.19	0.88	41.8	9.85	19.5*	d	--H-Z	-h	-c	-	19 01 35.2	06 51 30	0.4	...
J1901-04	30.10	-4.34	22.3	9.19	2.8*	-	--HSZ	-h	--	-
J1910+00	35.56	-3.98	22.3	9.12	2.4	d	--HSZ	-h	-c	-	19 10 24.9	00 32 21	1.4	...
J1912+13	47.26	1.46	39.9	9.49	10.4	-	--H-Z	-h	--	-
J1915+10	44.76	-0.49	11.5	8.80	43.7	-	--H-Z	-h	--	-
J1919+14	48.73	0.27	40.5	9.81	29.4	-	--H-Z	-h	--	n
J1921+14	49.58	0.23	57.4	9.74	19.5*	p	--H-Z	-h	-c	n	19 21 35.1	14 50 19	2.9	...
J1921+08	43.81	-2.91	43.9	9.37	3.7	d	--H-Z	-h	-c	-	19 22 00.2	08 18 24	1.6	...
J1922+18	53.12	1.82	55.5	10.10	11.6	d	--H--	-h	-c	-	19 22 45.8	18 42 40	2.6	...
...														
(b) HI-detections with more than one cross-match:														
J1929+08	44.43	-4.67	44.2	9.85	1.6	d	I-H-Z	-h	S-	n	19 29 19.8	08 02 42	1.0	DSH J1929.3+0802
						c	--H-Z	-h	Sc	n	19 29 19.9	08 04 46	3.0	DSH J1929.3+0804
J2143+46	92.71	-4.97	46.8	10.03	1.4	d	IM---	oh	N-	n	21 43 54.08	46 37 04.7	0.5	UGC 11802
						c	IM---	oh	N-	n	21 44 13.47	46 37 16.9	3.1	UGC 11806
...														
(c) HI detections with ambiguous cross-matches:														
J0213+66	31.09	4.66	59.9	9.83	4.0*	p	-----	--	-c	n	02 13 33.4	66 10 39	2.7	...
						a	-----	--	-c	n	02 13 11.5	66 12 28	2.4	...
J0636+00	10.41	-2.93	34.1	9.56	5.1	p	IMH-Z	-h	Nc	n	06 36 26.7	00 55 50	1.6	CGMW 1-0228
						a/c	-M---	--	N-	n	06 36 23.61	00 55 51.2	1.4	2MASX J06362361+0055513
...														

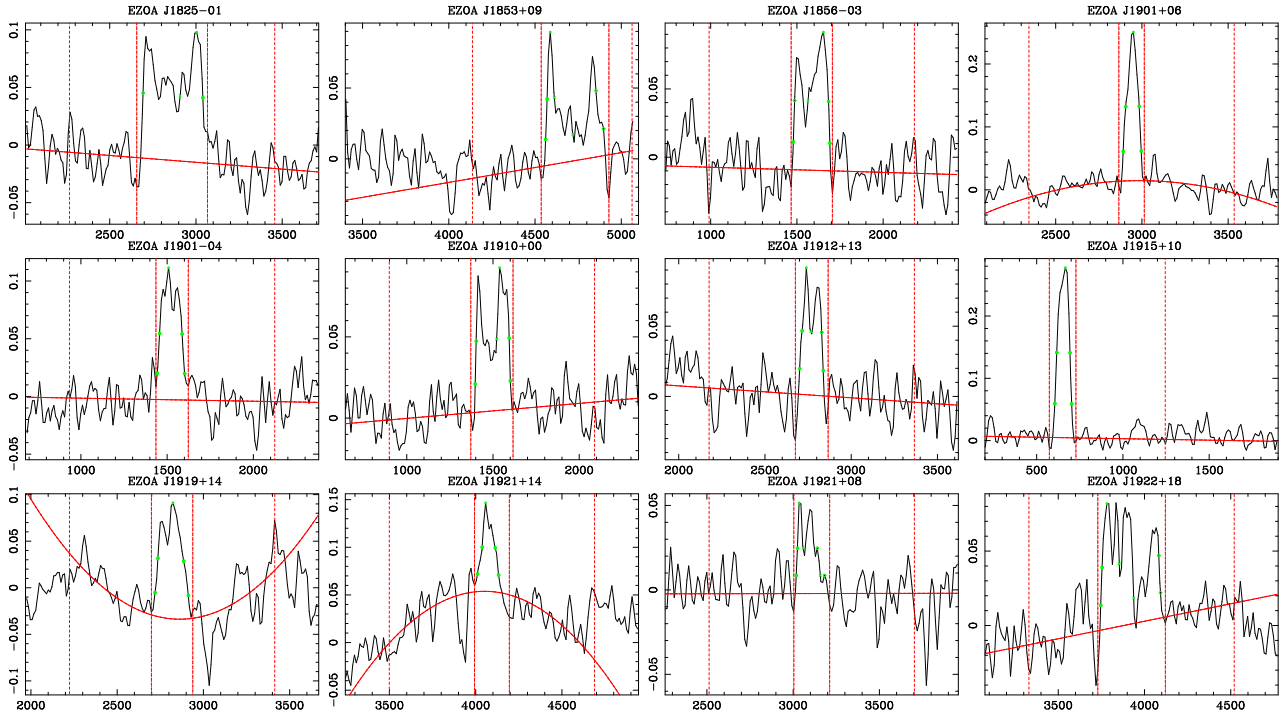


Figure 1. Example H I spectra of the newly detected galaxies in the EZOA blind survey (Flux densities, in Jy km s^{-1} , versus radial heliocentric velocity, in km s^{-1}); all the spectra are available online. Low order baselines (indicated by the solid line) are fitted, excluding the detections themselves (which are bracketed by the dash-dot vertical lines) and excluding the low and high-velocity edges to the left and right of the dashed vertical lines, respectively. 20% and 50% profile markers are visible.

4.1 Results of counterpart search

For 141 of the 170 HI detections we have found a cross-match (83%). In six cases (4%) more than one counterpart contributes to the HI signal. For three HI detections (2%) more than one galaxy candidate was found but no unambiguous counterpart could be decided on. The numbers are comparable to the cross-match rates listed in [Staveley-Smith et al. \(2016\)](#) for HIZOA-S. We have 67 new HI detections, that is, the rate of new HI detections is only 39% as compared to, e.g., 67% for HIZOA-S. This is understandable since the northern ZoA galaxies have been extensively observed with the Nançay, Arecibo and Effelsberg radio telescopes in targeted observations, and the northern ZoA is less severely affected by selection bias due to extinction than the southern part. This is also consistent with the fact that a fair fraction of the new detections, that is, 25% (or 19 detections) have no visible counterpart, which compares well with the 22% cited by [Staveley-Smith et al. \(2016\)](#) for HIZOA-S. On the other hand, of our 103 previously known HI detections only 12% (or 12 detections) have no visible counterpart; they all had been serendipitously detected in one of the less complete or less sensitive previous blind HI surveys. Finally, only 24 of the 67 previously HI undetected galaxies are published in a known galaxy catalogue.

Of the 147 cross-matched galaxies (where we count all of Table 3a and 3b, and only the first entry each in Table 3c), 99 (67%) are listed in NED or else in SIMBAD ($N_S = 3$). That means that 48 (33%) cross-matched galaxies are new, or in other words, they are not listed in the literature (at a wavelength other than HI) but were found by us on at least one of the searched images¹⁰. Figure 2 shows two examples: EZOA J2012+32 is a typical example of a galaxy at high extinctions, whereas EZOA J2131+43 is also visible at the optical passbands and was either missed in optical searches or the particular area was not covered.

There are 39 (27%) IRAS counterparts (plus one uncertain cross-match), 83 (56%) 2MASS counterparts, and 23 (16%) cross-matches have optical velocity measurements listed in the literature.

The median distance between the HI position and the actual counterpart (using only definite candidates and non-confused profiles, $N = 120$) is 1'.2, and 95% of the cross-matches are found within 3'.3 of the HI position. This compares well with the findings in [Staveley-Smith et al. \(2016\)](#), taking into account the difference in positional uncertainties and beam sizes and the smaller sample size.

5 COMPLETENESS AND RELIABILITY

Since our catalogue is of moderate size, we have determined a completeness limit for the survey as defined in [Donley et al. \(2005\)](#) for the northern extension of the HIZOA survey (HIZOA-N; $N = 77$). Figure 3 shows a histogram of the mean flux density S , that is, the flux integral divided by line width w_{20} . Where w_{20} was not available we added an offset of 24.5 km s^{-1} (as used in the error calculation, see Sec. 3)

to w_{50} . A nominal Euclidean power law, $N(S) \propto S_{\text{mean}}^{-2.5}$, laid by eye over the plot, shows clearly that the completeness limit must lie between 40 and 50 mJy (given the high scatter from the low numbers involved, together with the practical difficulties of fitting with substantial uncertainties in both axes, we considered the by-eye-fit to be sufficiently accurate). This limit coincides well with the median mean flux density of 47 mJy. Assuming a linear relationship between the peak flux and mean flux density, this corresponds to a median peak flux of 66 mJy, which is about 3σ above the nominal rms noise of the survey, 23 mJy.

5.1 Automated searches

With the upcoming large HI surveys to be conducted by the various SKA precursors as well as SKA itself, visual searches of the large and numerous data cubes are not feasible anymore. Various automated source detectors exist (e.g., [Whiting 2012](#), [Serra, Jurek & Flöer 2012](#), [Jurek 2012](#)), some of which are made available in the software package SoFiA ([Serra et al. 2015](#)). These have been extensively tested with simulations. However, real data deviates from simulated data mainly in non-uniform noise distribution, effects caused by RFI, the presence of continuum sources etc. In particular continuum sources, causing variations in the baseline which the automated source finders have difficulties dealing with, are a major problem in the ZoA (cf. Fig. 7 in [Staveley-Smith et al. 2016](#)). We were able to make some comparisons nonetheless.

5.1.1 Preliminary EBHIS shallow source catalogue

The preliminary EBHIS shallow source catalogue (described in [Flöer 2015](#)¹¹) was derived from a combination of an automated source finder, based on wavelet de-noising (also included in SoFiA, [Serra et al. 2015](#)), with an artificial neural network that determines whether a detected candidate is likely to be a real source. Details on the method can be found in [Flöer, Winkel & Kerp 2014](#), [Serra et al. 2015](#) and [Flöer & Winkel 2012](#). We describe the details of the comparison with our visual search in App. A since the neural network discriminator needs more balanced training systems to produce reliable results. Despite the caveats, a comparison is very useful since sources detected in one but not both searches give valuable feedback on the limitations of the respective search methods. In particular, we checked sources from the EBHIS shallow source catalogue that were not found in the visual searches. This approach added eventually three low-SNR detections (< 6) as well as one significant detection, EZOA J0637+03, which, however, lies on a strongly varying baseline and could only be confirmed through a cross-match with the HIZOA survey. No obvious source was missed which proves the thoroughness of visual searches.

5.1.2 The SOFIA package

We have also used the automated source finders in the software package SoFiA ([Serra et al. 2015](#)) to compare with our

¹⁰ They can be identified in Table 3 has having neither a name in Col. 13 nor an entry in the Col. 8 as having an HI counterpart (labelled as 'h').

¹¹ <http://hss.ulb.uni-bonn.de/2015/4227/4227.htm>

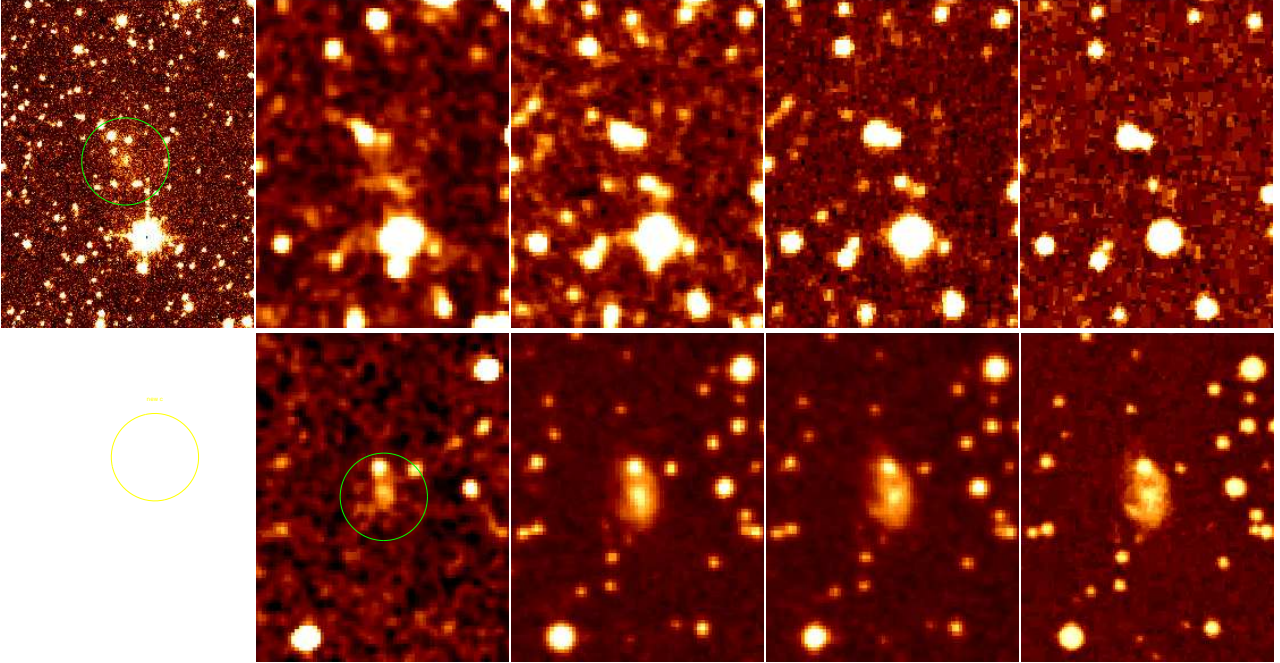


Figure 2. Two examples of galaxies not previously catalogued in visual searches. From left to right: UKIDSS K_s -band, 2MASS K_s -band, DSS I -band, DSS R -band and SuperCOSMOS B -band. Top: EZO J2012+32 at an extinction of $A_B = 8^m8$ is only visible in the deep K_s -band image. Bottom: EZO J2131+43 at a much lower extinction of $A_B = 1^m3$ is visible at all passbands (no deep K_s -band image exists to-date).

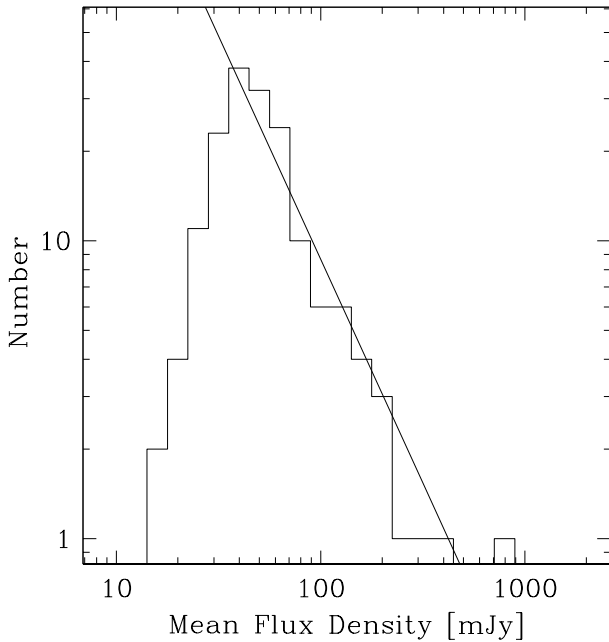


Figure 3. Log of the mean H I flux density S (flux integral divided by the line width w_{20}) for all 170 EZO detections. The black line corresponds to a slope of $-3/2$ that would be expected for a homogeneous distribution.

visual search, taking into account that SoFiA is still very much *under construction* and is affected by various software issues currently addressed (note that most of our testing was conducted on version 0.5).

SoFiA offers three different source finders in combination with three different filters. We have tested these (excluding the 2D-1D wavelet filter used for the aforementioned EBHIS source detection pipeline), with varying input parameter settings, on a single $12^\circ \times 12^\circ$ -cube¹². We found that none of the methods reliably detected sources, mainly due to non-straight baselines. This limitation is basically due to the fact that SoFiA has not been equipped with baseline subtraction which is obsolete for the interferometric data cubes for which SoFiA is primarily intended. However, the increased number of continuum sources in the ZoA introduces many artefacts that cannot be fully removed and which affect baselines also in interferometric data (Ramatsoku et al. 2016). In other words, real data cubes from the ZoA differ considerably from the averaged simulated interferometric cubes which were used to optimise the automated source finders. Baseline subtraction, whether performed on the cube before a source finder is used or during the search process, is a necessity for any kind of ZoA data cubes and needs to be addressed.

SoFiA also performs source parametrisation using input catalogues; it returned indeed most of our detections with improved positions and fitted H I parameters. Here we found that the recommended Smooth + Clip finder (Serra, Jurek & Flöer 2012) in combination with the Noise Scaling filter was the best choice by having the most complete return of input sources (Popping et al. 2012).

¹² We also used a HIZOA Parkes multibeam data cube (Staveley-Smith et al. 2016) as a test-set with similar results.

Table 4. Comparison of median rms and signal-to-noise ratio for different HI surveys

	EBHIS	HIZOA-S	HIPASS-S	HIPASS-N
rms:				
overall (average)	23 mJy	6 mJy	13 mJy	14 mJy
around detections	10.4 mJy ($N = 170$)	3.4 mJy ($N = 883$)	7.3 mJy ($N = 4315$)	7.7 mJy ($N = 1002$)
matches with HIPASS	10.1 mJy ($N = 37$)	—	8.5 mJy ($N = 37$)	
non-matches with HIPASS	9.1 mJy ($N = 14$)	—	—	
rms _{detected} : rms _{overall}	0.45	0.57	0.56	0.55
SNR:				
detections	7.2 ($N = 170$)	10.4 ($N = 883$)	8.5 ($N = 4315$)	8.0 ($N = 1002$)
matches with HIPASS	8.0 ($N = 37$)	—	9.1 mJy ($N = 37$)	
non-matches with HIPASS	6.1 ($N = 14$)	—	—	

5.2 Comparison with other HI surveys

During our visual search, we used the more sensitive HIZOA catalogues to confirm doubtful detections in the overlap region ($-5^\circ \leq \delta \leq +25^\circ$) and to ensure that no source was overlooked. Only four sources were not found in our initial search, all with an SNR between 5 and 7 and all affected by varying baselines.

As a fully independent check, we compared our final list of detections with HIPASS (HI Parkes All Sky Survey), which is a blind HI survey of the full southern hemisphere plus a northern extension at an intermediate sensitivity (rms = 13 – 14 mJy), also conducted with the Parkes radio telescope (Meyer et al. 2004; hereafter HIPASS-S; Wong et al. 2006; hereafter HIPASS-N). There are 39 detections in common: 27 from HIPASS-S and 11 from HIPASS-N, with one further detection recorded in the bright galaxy catalogue, which is based on an older version of the HIPASS-S catalogue (Koribalski et al. 2004).

For the completeness check, we have looked at all HIPASS sources that we have not detected. Most of these were indeed too faint for our survey, that is, their peak flux density is < 50 mJy. The brightest, with a peak of ~ 100 mJy (HIPASS J1917+11), is near a continuum source and was thus not detected by us. Four HIPASS sources with peak flux densities ranging from 60 – 90 mJy are visible in the EBHIS cubes but they are not distinctly distinguishable from noise. We conclude that our search did not miss any significant detections.

For the reliability check, we looked at the 14 EZOA detections in the overlap region with HIPASS which were not detected by HIPASS. We cross-checked each position with the HIPASS data archive¹³ and find that five of the detections show strong baseline variations in HIPASS, which likely affected the automated HIPASS source detection, seven are visible but have clearly a low signal-to-noise ratio, and two show obvious profiles (EZOA J0552+22 and EZOA J0640–01).

To explore why the sources were not detected with the more sensitive HIPASS, we have compared the rms (after baseline fitting) around HI detections for the four surveys EZOA, HIZOA-S (Staveley-Smith et al. 2016), HIPASS-S and HIPASS-N, see Table 4. As expected, the rms around detected sources tends to be smaller than the average rms

across a full survey: e.g., whereas the overall rms of the HIZOA-S survey is 6 mJy, the median rms around the detected sources is only 3.4 mJy. If we calculate the ratio of these ‘detected’ rms values with the overall rms, we find that the ratio is slightly lower for EZOA (0.45 versus 0.57, 0.56 and 0.55 for the three other surveys, respectively).

We can also compare the SNR: While the median SNR for HIZOA-S is high at 10.4 (this survey used deliberately a high cut-off with the aim to be reliable), the median SNR of EZOA at 7.2 is also lower than for HIPASS, albeit marginally so (8.5 for HIPASS-S and 8.0 for HIPASS-N), as one would expect for a visual versus automated search.

The 14 EZOA detections not detected by HIPASS have a slightly lower median rms and also a lower median SNR than the average, indicating that they were only found with EBHIS because they are in low-rms areas (for example, overlap regions in the mosaiced survey). Furthermore, 11 of these detections are in the HIPASS-N region where the intrinsic rms is higher due to the low elevation of the Parkes radio telescope (cf. discussion in Wong et al. 2006).

5.3 Source parameters

We compared the extracted HI parameters with published values. We found reasonable overlap with HIPASS ($N = 38$), HIZOA ($N = 32$) and Nançay radio telescope measurements (NRT; $N = 35$) (Kraan-Korteweg et al. 2018; Paturel et al. 2003; Theureau et al. 1998; Chamaraux et al. 1990; Martin et al. 1990). For the comparison we excluded obviously confused cases. Table 5 gives the mean difference in the parameter, the median and the standard deviation for the detections in common (i.e., where the parameters were available; note that for HIPASS we use their width-maximised v_{50} , w_{50} and w_{20}). No statistically significant systematic effects (i.e., at the 3σ level) are noticeable except for the marginal case of the flux comparison with HIZOA which improves to a mean of -13.3 ± 5.9 when only sources with $\text{SNR} > 6$ are used.

5.3.1 Automated source finders

The EBHIS preliminary shallow source catalogue lists all HI parameters. They compare well with our parameters except for an offset in w_{20} which is due to the fact that we used handning smoothed data; since the catalogue is only preliminary we will not go further into details.

¹³ <http://www.atnf.csiro.au/research/multibeam/release>

Table 5. Comparison of EZOA parameters

Parameter [unit]	N	Mean	Median	Std dev
a) HIPASS (PKS)				
v_{50} [km s ⁻¹]	36	-1.3 ± 2.2	- 1.1	13.0
w_{50} [km s ⁻¹]	35	-9.6 ± 5.1	- 3.6	29.9
w_{20} [km s ⁻¹]	30	-10.3 ± 8.5	- 5.5	46.5
Flux integral [%]	36	-13.6 ± 6.4	- 7.8	38.2
b) various NRT				
v_{50} [km s ⁻¹]	35	0.1 ± 1.3	0.0	7.8
w_{50} [km s ⁻¹]	32	6.1 ± 4.3	3.0	24.4
w_{20} [km s ⁻¹]	32	1.3 ± 5.3	6.5	29.8
Flux integral [%]	34	8.5 ± 5.2	10.5	30.2
c) HIZOA (PKS)				
v_{50} [km s ⁻¹]	31	-2.3 ± 1.7	0.0	9.6
w_{50} [km s ⁻¹]	31	0.6 ± 5.4	10.0	30.0
w_{20} [km s ⁻¹]	27	8.0 ± 5.7	15.0	29.8
Flux integral [%]	31	-20.5 ± 6.3	- 17.1	35.3
e) SoFiA (for $w_{50} < 200$ km s ⁻¹)				
v_{50} [km s ⁻¹]	109	-0.6 ± 1.6	- 3.0	16.8
w_{50} [km s ⁻¹]	109	8.2 ± 2.7	8.0	28.6
w_{20} [km s ⁻¹]	97	6.2 ± 3.1	11.0	30.2
Flux integral [%]	109	-4.3 ± 8.6	6.8	90.0

Since we were able to extract most of the sources found in the visual search with SoFiA we investigated the source parameters from the most successful run using the Smooth + Clip finder and the Noise Scaling filter. Though the velocities compare well, the line width measurements are highly affected by the size allocated by SoFiA for parametrisation being restricted to 22 pixel (that is, in the case of EBHIS only about 225 km s⁻¹). This feature is being addressed by the SoFiA developers. Hence, for the comparison we used only detections with $w_{50} < 200$ km s⁻¹, see the last entry in Table 5. The parameters now compare well, only w_{50} shows a 3σ offset.

Since H I positions of single dish observations have large uncertainties due to the large beam size, we wanted to know if the accuracy of the source position varies depending on the parametrisation algorithm. For the comparison, we have used the positions of the optical/NIR counterparts (Sec. 4). While the positions read off visually from the cubes are understandably less accurate (these positions were usually chosen as the (x,y) -pixel where the profile has its peak), the positions from the MIRIAD and SoFiA fits as well as the positions in the EBHIS catalogue are of comparable precision. Table 6 lists the mean, median and standard deviation of the distribution in distance between the counterpart and H I position (in arcminutes) for definite candidates and non-confused profiles ($N = 120$).

These comparisons give an idea on how the parameters may vary when a different software is used, whereas a comparison with the literature points out differences due to instrument and observing strategies. Table 5 shows that there are no significant differences (beyond the one exception mentioned above) and we conclude that variations in the data (with telescope and instrument settings) do not increase the uncertainties in the parameters.

Table 6. Comparison of H I position accuracy using optical and NIR cross-matches

Method	N	Mean	Median	Std dev
Visual	120	1'92 ± 0'09	1'75	1'01
MIRIAD	120	1'54 ± 0'11	1'22	1'22
SoFiA	117	1'46 ± 0'09	1'24	0'97
EBHIS	64	1'49 ± 0'14	1'18	1'11

6 HI PROPERTIES OF THE SAMPLE

To characterise the H I properties of our sample, we present some of the parameters in Fig. 4. The top panel shows the recessional velocities in the Local Group frame of reference. Though the survey's sensitivity drops off quickly for $\gtrsim 5000$ km s⁻¹, there is a pronounced peak at 4000 km s⁻¹ which is clearly due to large scale structures (see discussion in Sec. 7). The next panel shows the distribution of H I masses, ranging from $\log(M_{\text{HI}}) = 7.0$ (for EZOA J0630+08 at $v_{\text{LG}} = 250$ km s⁻¹, no counterpart visible but detected by HIPASS and HIZOA) to 10.6 (for EZOA J2204+48 at $v_{\text{LG}} = 11,66$ km s⁻¹ with an edge-on visible galaxy not recorded in the literature as counterpart; the SNR, however, is only 6.7). The mean is 9.6 and the median is 9.8.

The distribution of line widths measured at half peak, w_{50} , is highly skewed with a peak at ~ 100 km s⁻¹, a mean of 176 km s⁻¹ and a median of 146 km s⁻¹, very similar to the HIZOA-S survey (with a mean and median of 163 km s⁻¹ and 147 km s⁻¹, respectively). It is interesting to note that the line width distribution of a pointed survey of NIR-selected targets, as, for example, presented by (Kraan-Korteweg et al. 2018), shows a more Gaussian distribution with a higher mean of 288 km s⁻¹ that is the same as the median, as shown in Fig. 5 as the filled green histogram. It is obvious that many galaxies with narrow line widths (often low-surface brightness dwarf galaxies) are missed in the pointed observations. This is likely due to the high Galactic foreground extinction and the low sensitivity of the NIR to late type spirals and irregular galaxies which means they rarely appear in NIR-selected samples in the ZoA.

The iteratively-clipped rms noise around each detection is shown in the bottom panel. Whereas the overall rms of the EBHIS survey is 23 mJy, the rms around the detections, as discussed in Sec. 5.2, is considerably lower, partly due to the clipping but also because the overall rms refers to the full velocity range ($-600 < cz < 18000$ km s⁻¹) while most of our detections are below 6000 km s⁻¹. The histogram also shows a considerable contribution from very low-rms detections most of which are located in the overlap regions between the mosaiced scans.

Figure 6 shows the distribution of H I mass as a function of velocity in the Local Group frame for the EZOA and HIPASS-S detections. The low statistics of the EZOA sample makes a comparison difficult, but the overall shape of the distributions are comparable and no undue outliers are apparent.

Two notable detections are the one with the lowest H I mass and the one with the largest line width. The lowest H I mass ($\log(M_{\text{HI}}) = 7.0$) was measured for EZOA J0629+08 at $v_{\text{LG}} = 250$ km s⁻¹ for which no counterpart could be found; it was detected, however, in the HIPASS and HIZOA

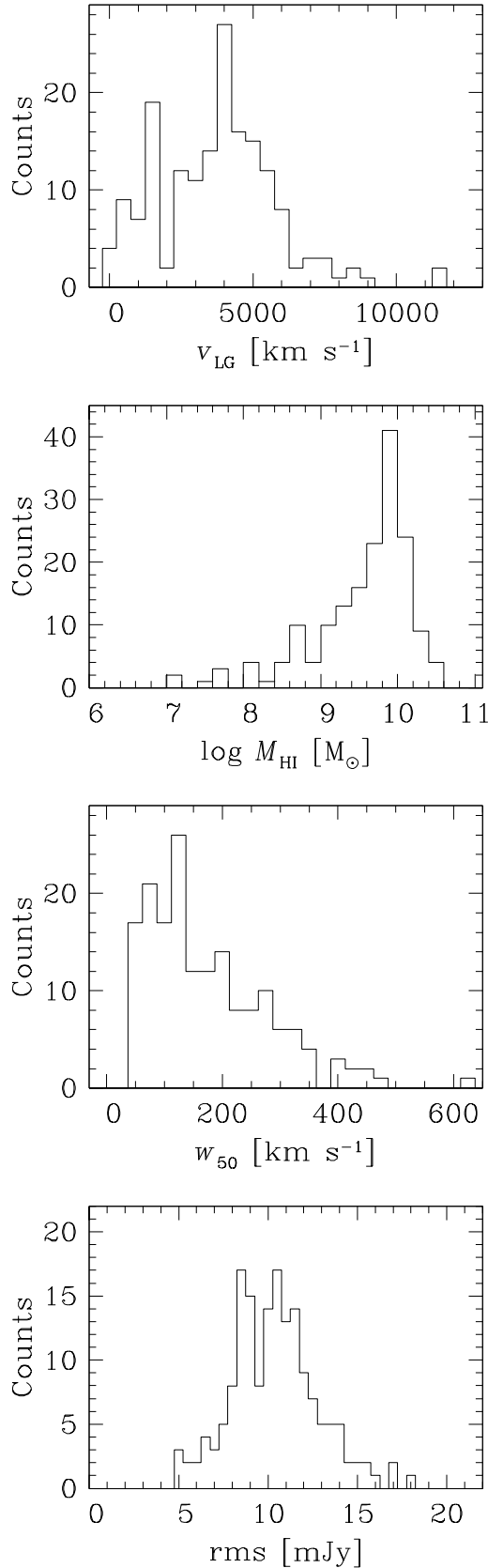


Figure 4. HI parameters of the 170 detections in the EZOA survey. From top to bottom the histograms display the radial velocity v_{LG} , the HI-mass distribution, the line width w_{50} , and the clipped rms noise at the position of the detected galaxy.

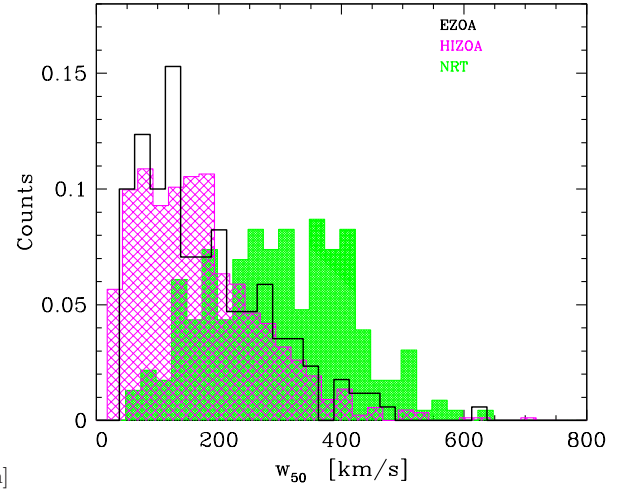


Figure 5. HI line width distribution: the two blind surveys EZOA (black open histogram) and HIZOA (hashed magenta) are compared to a NIR-selected survey (green filled histogram) conducted with the NRT (Kraan-Korteweg et al. 2018).

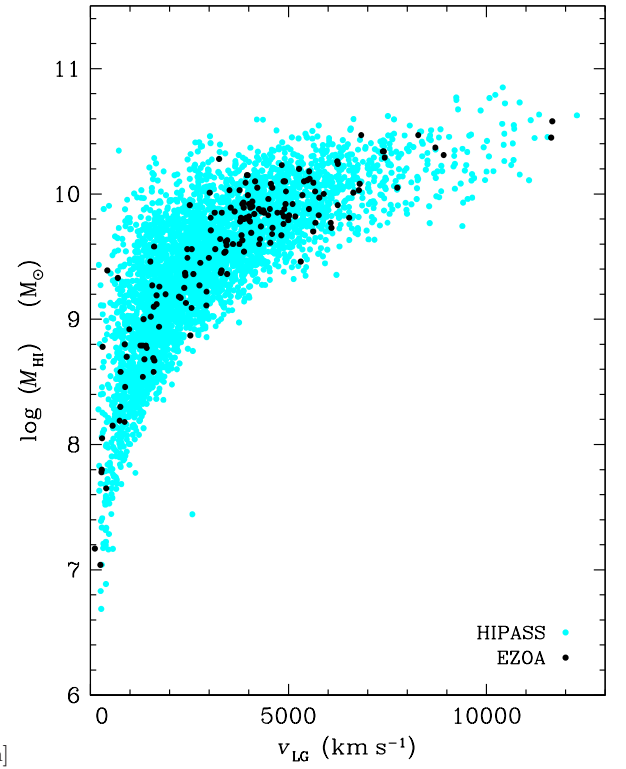


Figure 6. HI mass versus velocity in the Local Group frame for the EZOA (black) and HIPASS samples (light blue; Meyer et al. 2004).

surveys. The largest line width ($w_{50} = 616 \text{ km s}^{-1}$) belongs to a marginal detection (EZOA J0358+54) with no visible counterpart (it has a high extinction of $A_B = 6^m.7$).

7 LARGE-SCALE STRUCTURE ANALYSIS

Despite the low sensitivity of the shallow EBHIS survey, 39% of the HI detections are new ($N = 67$), and only five of these

have previously recorded optical redshifts. Twenty-six of the new H I detections have a visible counterpart *not* previously recorded in the literature, and a further 17 have no visible counterpart so far (likely due to a mix of difficult to find low-surface brightness galaxies and the higher extinction in the survey region). In addition, 34 of those detections which already have been recorded in existing H I catalogues have also no optical or NIR counterpart in the literature, though in 22 of these cases we found such a counterpart on at least one of the images we searched. Though the numbers of new galaxies are small, they show the power of systematic blind H I surveys in the ZoA.

7.1 Nearby galaxies

Fifteen of our detections are found within 11 Mpc, six of which belong to the Maffei group (Karachentsev 2005). Three detections were not observed in H I before, and four have no optical or NIR counterpart. The 15 detections are dominated by dwarf galaxies: the H I masses range from $\log(M_{\text{HI}}) = 7.0$ to 9.4, with a median of 8.1. The line widths are also considerably smaller, with a median of $w_{50} = 94 \text{ km s}^{-1}$ as compared to 146 km s^{-1} for the full catalogue.

No previously unidentified galaxy was found in this volume, proving that there is no hidden massive galaxy in the northern sky that would significantly influence the motion of the Local Group with respect to the microwave background.

7.1.1 Closest detection: IC 10

The closest detection is that of IC 10 (EZO J0020+59) at $v_{\text{HI}} = -346 \text{ km s}^{-1}$; the velocity with respect to the Local Group is -84 km s^{-1} . We adopt 0.74 Mpc for its distance, as determined by Tully et al. (2013) based on measurements of Cepheids and the tip of the red giant branch. Our velocity agrees well with the range found in the literature ($\sim -352 - -342 \text{ km s}^{-1}$). The H I emission covers at least 23 frames in the cube, and it is likely that a more meticulous extraction of the profile would improve the parameters.

7.1.2 HIZSS 003

The second closest detection in our catalogue (EZO J0700-04) is HIZSS 003 which was only recently detected in the Parkes HIZOA Shallow Survey (Henning et al. 2000). Begum et al. (2005) observed this galaxy with the VLA and found that the H I emission comes from two dwarf galaxies. Both are faintly visible on the deep NIR images; we give their coordinates in our cross-match table. Together with EZO J0630+08 it is the least massive dwarf in our catalogue ($\log(M_{\text{HI}}) = 7.1$ and 7.0, respectively).

7.1.3 Maffei group

The Maffei group (e.g., Karachentsev 2005) consists of the IC 342 subgroup and the Maffei 1 subgroup; only the Maffei 1 subgroup lies deep in the plane and was thus detected by us. Of the 8 known members in the Maffei 1 subgroup, we have detected six: Dwingeloo 1 and 2, KK 11 and 12, Maffei 2 and MB 3. We did not detect MB 1 ($v_{\text{HI}} = 59 \text{ km s}^{-1}$, Huchtmeier, Karachentsev & Karachentseva 2003) since it

is faint and close to Dwingeloo 1 (as well as to the Galactic H I). Maffei 1 is an S0 galaxy and has not been detected in H I. A ninth, possible member (KKH 6) lies outside our search area. No new member was uncovered.

7.1.4 New H I detections at $D < 11 \text{ Mpc}$

Of particular interest is EZO J2120+45 or 2MASX J21204618+4516221 which lies in the Local Volume at a distance of 7.5 Mpc and was not detected in H I before. Its H I mass is $\log M_{\text{HI}} = 8.2$. In addition, EZO J0506+31 and EZO J0301+56, at the edge of the local volume at 10.1 Mpc are newly found galaxies. Both are dwarf galaxies at $\log M_{\text{HI}} = 8.3$ and 8.6, respectively. EZO J0301+56 does not have an optical counterpart.

7.2 Large-scale structures

Figure 7 shows the distribution of the 170 H I detections in Galactic coordinates colour-coded by velocity (middle panel). For interest, we also show the velocity measurements available in the literature, using HyperLEDA (status March 2019, using `objtype = 'G'`), top panel, and our new detections added in, bottom panel. Two features are immediately obvious: the Supergalactic plane (SGP, at $l \sim 140^\circ$) has been more firmly established, and the empty patch at around $60^\circ < l < 80^\circ$ and $-5^\circ < b < +1^\circ$ has been filled. We discuss these and other features in detail below, using plots of individual redshift slices that cover a larger area ($260^\circ > l > 24^\circ$, $|b| \leq 25^\circ$; Figs 8 and 9) where individual large scale structures can be traced more easily.

Figure 8 shows the nearby galaxies up to 2000 km s^{-1} . Though the number of detections in this slice is small ($N = 40$), both aforementioned features are present:

(1) At $140^\circ < l < 150^\circ$, the connection of the Supergalactic Plane across the ZoA shows six new galaxies in the narrow velocity range $1350 \text{ km s}^{-1} < v < 1750 \text{ km s}^{-1}$, three of which have no optical counterpart. Just above our search area, at $b \sim 12^\circ$, are three known galaxy groups at similar velocities (HDC 248, Crook et al. 2007, [TSK2008] 0139 and [TSK2008] 0141, Tully et al. 2008). The new galaxies seem to be part of a filament connecting these groups into and possibly across the ZoA towards the south.

(2) The previously empty patch around $l \sim 70^\circ$ shows three new galaxies with $980 < v < 1530 \text{ km s}^{-1}$. It looks like a continuation of a filament below the ZoA but a deeper survey is required to strengthen this connection.

Figure 9 shows galaxies between 2000 and 5000 km s^{-1} ; there are 92 detections in total. The two features mentioned above are also prominent in this slice, but there are other noticeable structures as well.

(3) The innermost ZoA gap of the SGP at $l \sim 140^\circ$, that is, between $b = 0^\circ$ and $b = -2^\circ$, is now filled in both redshift bins.

(4) The previously empty patch around $l \sim 70^\circ$ shows seven detections, with four having redshifts in the very narrow redshift range $3380 - 3460 \text{ km s}^{-1}$, possibly indicating a new filament crossing the ZoA from South-East to North-West – again, more data is required to make a definite statement. One of these galaxies was also detected by HIPASS (it does not appear in the HyperLEDA sample since it was la-

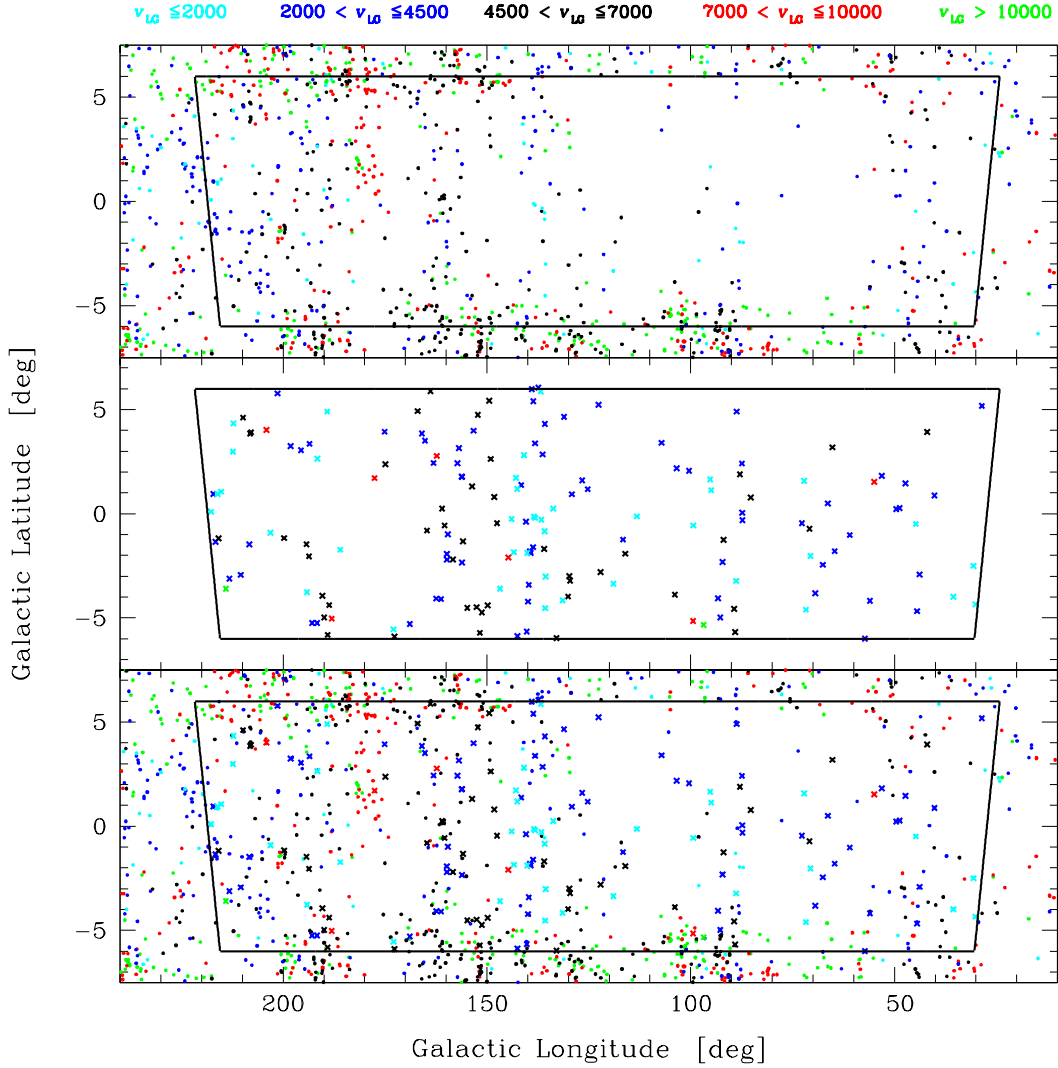


Figure 7. Distribution of galaxies with velocity measurements in Galactic coordinates. Top panel: distribution of galaxies available through HyperLEDA; middle panel: distribution of the 170 HI-detected galaxies; bottom panel: both distributions are shown together. The survey area is indicated by the dashed line ($\delta \leq -5^\circ$, $|b| < 6^\circ$). The symbols are colour-coded as a function of velocity. Note the predominance of galaxies around $\ell \sim 150^\circ$ and $\ell \sim 90^\circ$.

belled ‘HI’ and not as a galaxy, having no published optical counterpart). All seven galaxies are visible in the NIR.

(5) The tail-end of the Perseus–Pisces filament that crosses the ZoA in Cygnus at $l \sim 90^\circ$ and which has been discussed extensively by Ramatsoku et al. (2016) and Kraan-Korteweg et al. (2018), has also been strengthened despite the drop in sensitivity of our survey for redshifts above 4000 km s^{-1} .

(6) In the area of $150^\circ < \ell < 170^\circ$, two filaments at different redshifts, seemingly crossing each other, have obtained more galaxies: the lower-redshift filament crosses from South-East to North-West and seems to go parallel to the SGP. The higher-redshift filament crosses from South-West to North-East, that is, from the Perseus clus-

ter ($v \sim 5400 \text{ km s}^{-1}$) towards the intermediate-rich galaxy cluster ZwCl0731.9+3125 ($v \sim 4550 \text{ km s}^{-1}$). It is possibly another branch of the Perseus–Pisces filament, curving back towards lower velocities, whereas the other branch continues strictly North and outward, that is, through $\ell = 160^\circ$ ($v \sim 6000 \text{ km s}^{-1}$) to Abell 569 ($v \sim 5900 \text{ km s}^{-1}$) (Kraan-Korteweg et al. 2018).

(7) Another noticeable structure in our plot, though we have not added any new data here, is a tenuous filament at around $v \sim 3000 \text{ km s}^{-1}$, crossing the ZoA at $40^\circ < \ell < 50^\circ$ in a North–South direction.

While the Perseus–Pisces supercluster is one of the largest and most prominent large-scale structures in the northern sky, it lies just outside the sensitivity of our survey

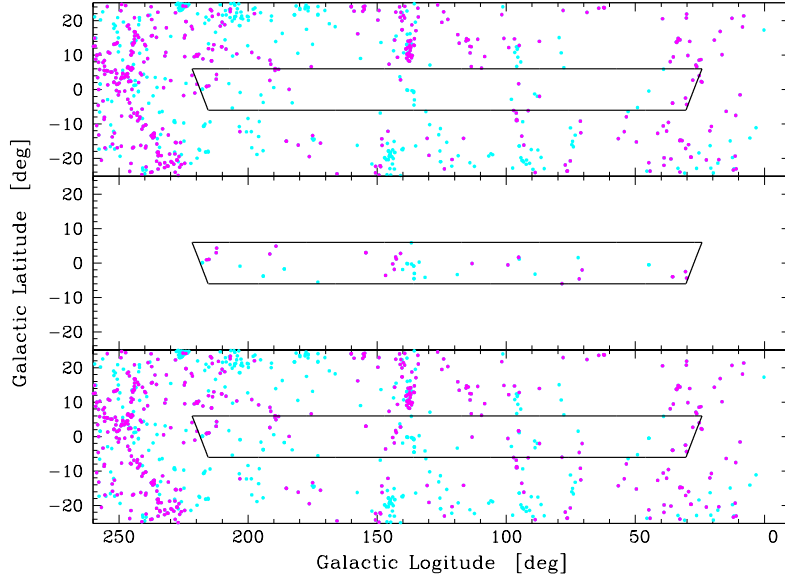


Figure 8. Same as Fig. 7 for nearby galaxies: light blue: $v_{\text{LG}} < 1000 \text{ km s}^{-1}$; magenta: $1000 \text{ km s}^{-1} < v_{\text{LG}} < 2000 \text{ km s}^{-1}$.

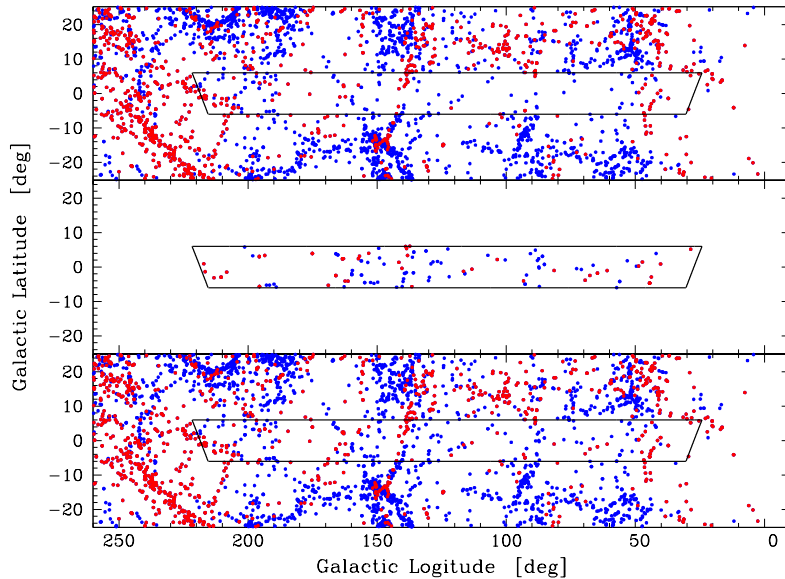


Figure 9. Same as Fig. 7 for galaxies at intermediate velocities: red: $2000 \text{ km s}^{-1} < v_{\text{LG}} < 3500 \text{ km s}^{-1}$; blue: $3500 \text{ km s}^{-1} < v_{\text{LG}} < 5000 \text{ km s}^{-1}$.

($v > 5000 \text{ km s}^{-1}$). We will, however, be able to trace it with the upcoming full EBHIS survey.

8 SUMMARY AND CONCLUSIONS

We used the first pass of the EBHIS survey (with a sensitivity of 23 mJy beam^{-1} at a velocity resolution of 10.24 km s^{-1}) to extract a catalogue of galaxies in the north-

ern ZoA ($\delta \geq -5^\circ$ and $|b| < 6^\circ$). We have found 170 detections in HI, 67 of which are new detections and only 24 of these were previously recorded in the literature as (optical) galaxies. These numbers demonstrate the power of blind HI surveys in searching for galaxies in the ZoA, and even more so since the here-presented survey is only a very shallow one.

The EZOA HI parameters and positions are of good quality: they compare well with the literature and other source parametrising algorithms. The positional 1σ uncer-

tainty is found to be 1:2, with 95% of the cross-matches lying within 3'3 of the HI position.

Blind HI surveys and pointed surveys of optical or NIR selected targets in the ZoA differ significantly in the HI line width distribution. Whereas the pointed observations show nearly a Gaussian distribution with a mean of $w_{50} \sim 300 \text{ km s}^{-1}$, blind surveys find many more narrow-line-width detections which often come from low-surface brightness dwarf galaxies that are rarely visible at higher Galactic extinction levels and are thus missed in pointed observations of an optical or NIR selected sample. Thus, we have found two new dwarf galaxies located at the edge of the Local Volume at 10.1 Mpc.

With 62 new redshift measurements in the 2280 square-degree northern ZoA strip, we find that most prominent large-scale structures crossing this strip have been established more firmly. We also found new galaxies in a previously empty region around 70° in Galactic longitude and slightly below the Galactic plane. The full EBHIS survey, which will be available in 2020 and will have a sensitivity comparable to the HIPASS survey in the South, will be most valuable for the ZoA research and the full-sky cosmic flow analyses by filling in the still persistent gap in the northern ZoA.

ACKNOWLEDGEMENTS

This research has made use of: the HyperLEDA database; the NASA/IPAC Extragalactic Database (NED) which is operated by the Jet Propulsion Laboratory, California Institute of Technology, under contract with the National Aeronautics and Space Administration; the SIMBAD database, operated at CDS, Strasbourg, France; the SuperCOSMOS Sky Surveys; the WFCAM and VISTA Science Archives, operated at the Royal Observatory of Edinburgh (WFAU); the Sloan Digital Sky Survey which is managed by the Astrophysical Research Consortium for the Participating Institutions. ACS thanks the South African NRF for their financial support.

REFERENCES

- Begum A., Chengalur J. N., Karachentsev I. D., Sharina M. E., 2005, *MNRAS*, 359, L53
- Chamaroux P., Cayatte V., Balkowski C., Fontanelli P., 1990, *A&A*, 229, 340
- Courtois H. M., Tully R. B., Fisher J. R., Bonhomme N., Zavodny M., Barnes A., 2009, *AJ*, 138, 1938
- Crook A. C., Huchra J. P., Martimbeau N., Masters K. L., Jarrett T., Macri L. M., 2007, *ApJ*, 655, 790
- Donley J. L., Staveley-Smith L., Kraan-Korteweg R. C., Islas-Islas J. M., Schröder A., et al., 2005, *AJ*, 129, 220
- Duffy A. R., Meyer M. J., Staveley-Smith L., Bernyk M., Croton D. J., Koribalski B. S., Gerstmann D., Westerlund S., 2012, *MNRAS*, 426, 3385
- Flöer L., 2015, Automated source extraction for the next generation of neutral hydrogen surveys, PhD Thesis, University of Bonn
- Flöer L., Winkel B., 2012, *Publ. Astron. Soc. Australia*, 29, 244
- Flöer L., Winkel B., Kerp J., 2014, *A&A*, 569, A101
- Gooch R., 1996, in *Astronomical Society of the Pacific Conference Series*, Vol. 101, *Astronomical Data Analysis Software and Systems V*, Jacoby G. H., Barnes J., eds., p. 80
- Haynes M. P., Giovanelli R., et al., 2018, *ApJ*, 861, 49
- Helou G., Walker D. W., 1988, in *NASA RP-1190*, Vol. 7 (1988), Vol. 7
- Henning P. A., Kraan-Korteweg R. C., Rivers A. J., Loan A. J., Lahav O., Burton W. B., 1998, *AJ*, 115, 584
- Henning P. A. et al., 2008, in *American Institute of Physics Conference Series*, Vol. 1035, *The Evolution of Galaxies Through the Neutral Hydrogen Window*, Minchin R., Momjian E., eds., pp. 246–248
- Henning P. A. et al., 2000, *AJ*, 119, 2686
- Hill G. J., Heasley J. N., Becklin E. E., Wynn-Williams C. G., 1988, *AJ*, 95, 1031
- Huchra J. P., Macri L. M., Masters K. L., Jarrett T. H., Berlind P., Calkins M., 2012, *ApJS*, 199, 26
- Huchtmeier W. K., Karachentsev I. D., Karachentseva V. E., 2003, *A&A*, 401, 483
- Jarrett T. H., Chester T., Cutri R., Schneider S., Skrutskie M., Huchra J. P., 2000, *AJ*, 119, 2498
- Johnston S. et al., 2008, *Experimental Astronomy*, 22, 151
- Juraszek S. J. et al., 2000, *AJ*, 119, 1627
- Jurek R., 2012, *Publ. Astron. Soc. Australia*, 29, 251
- Kalberla P. M. W., Mebold U., Reif K., 1982, *A&A*, 106, 190
- Karachentsev I. D., 1980, *ApJS*, 44, 137
- Karachentsev I. D., 2005, *AJ*, 129, 178
- Kerp J., Winkel B., Ben Bekhti N., Flöer L., Kalberla P. M. W., 2011, *Astronomische Nachrichten*, 332, 637
- Kerr F. J., Lynden-Bell D., 1986, *MNRAS*, 221, 1023
- Koribalski B. S., 2012, *PASA*, 29, 359
- Koribalski B. S. et al., 2004, *AJ*, 128, 16
- Kraan-Korteweg R. C., van Driel W., Schröder A. C., Ramatsoku M., Henning P. A., 2018, *MNRAS*, 481, 1262
- Kronberger M. et al., 2006, *A&A*, 447, 921
- Lang R. H. et al., 2003, *VizieR Online Data Catalog*, 734, 20738
- Li D., Nan R., Pan Z., 2013, in *IAU Symposium*, Vol. 291, *Neutron Stars and Pulsars: Challenges and Opportunities after 80 years*, van Leeuwen J., ed., pp. 325–330
- Martin J. M., Bottinelli L., Dennefeld M., Fouque P., Gouguenheim L., Patrel G., 1990, *A&A*, 235, 41
- Masters K. L., Crook A., Hong T., Jarrett T. H., Koribalski B. S., Macri L., Springob C. M., Staveley-Smith L., 2014, *MNRAS*, 443, 1044
- McIntyre T. P., Henning P. A., Minchin R. F., Momjian E., Butcher Z., 2015, *AJ*, 150, 28
- Meyer M. J. et al., 2004, *MNRAS*, 350, 1195
- Nan R. et al., 2011, *International Journal of Modern Physics D*, 20, 989
- Oosterloo T., Verheijen M., van Cappellen W., 2010, in *ISKAF2010 Science Meeting*, p. 43
- Patrel G., Theureau G., Bottinelli L., Gouguenheim L., Coudreau-Durand N., Hallet N., Petit C., 2003, *A&A*, 412, 57
- Popping A., Jurek R., Westmeier T., Serra P., Flöer L., Meyer M., Koribalski B., 2012, *Publ. Astron. Soc. Australia*, 29, 318
- Ramatsoku M. et al., 2016, *MNRAS*, 460, 923
- Rebull L. M. et al., 2011, *ApJS*, 196, 4
- Riad I. F., Kraan-Korteweg R. C., Woudt P. A., 2010, *MNRAS*, 401, 924
- Rivers A. J., Henning P. A., Kraan-Korteweg R. C., 1999, *Publ. Astron. Soc. Australia*, 16, 48
- Rosenberg J. L., Schneider S. E., 2000, *ApJS*, 130, 177
- Sault R. J., Teuben P. J., Wright M. C. H., 1995, in *Astronomical Society of the Pacific Conference Series*, Vol. 77, *Astronomical Data Analysis Software and Systems IV*, Shaw R. A., Payne H. E., Hayes J. J. E., eds., p. 433
- Schlafly E. F., Finkbeiner D. P., 2011, *ApJ*, 737, 103

- Schlegel D. J., Finkbeiner D. P., Davis M., 1998, *ApJ*, 500, 525
 Schröder A. C., van Driel W., Kraan-Korteweg R. C., 2019, *MNRAS*, 482, 5167
 Seeberger R., Huchtmeier W. K., Weinberger R., 1994, *A&A*, 286, 17
 Seeberger R., Saurer W., 1998, *A&AS*, 127, 101
 Serra P., Jurek R., Flöer L., 2012, *Publ. Astron. Soc. Australia*, 29, 296
 Serra P. et al., 2015, *MNRAS*, 448, 1922
 Springob C. M., Haynes M. P., Giovanelli R., Kent B. R., 2005, *ApJS*, 160, 149
 Staveley-Smith L., Davies R. D., 1987, *MNRAS*, 224, 953
 Staveley-Smith L., Kraan-Korteweg R. C., Schröder A. C., Henning P. A., Koribalski B. S., Stewart I. M., Heald G., 2016, *AJ*, 151, 52
 Strauss M. A., Huchra J. P., Davis M., Yahil A., Fisher K. B., Tonry J., 1992, *ApJS*, 83, 29
 Takata T., Yamada T., Saito M., Chamaraux P., Kazes I., 1994, *A&AS*, 104, 529
 Theureau G., Bottinelli L., Coudreau-Durand N., Gouguenheim L., Hallet N., Loulergue M., Paturol G., Teerikorpi P., 1998, *A&AS*, 130, 333
 Tully R. B. et al., 2013, *AJ*, 146, 86
 Tully R. B., et al., 2008, *ApJ*, 676, 184
 Whiting M. T., 2012, *MNRAS*, 421, 3242
 Winkel B., Kalberla P. M. W., Kerp J., Flöer L., 2010, *ApJS*, 188, 488
 Winkel B., Kerp J., Flöer L., Kalberla P. M. W., Ben Bekhti N., Keller R., Lenz D., 2016, *A&A*, 585, A41
 Wong O. I. et al., 2006, *MNRAS*, 371, 1855

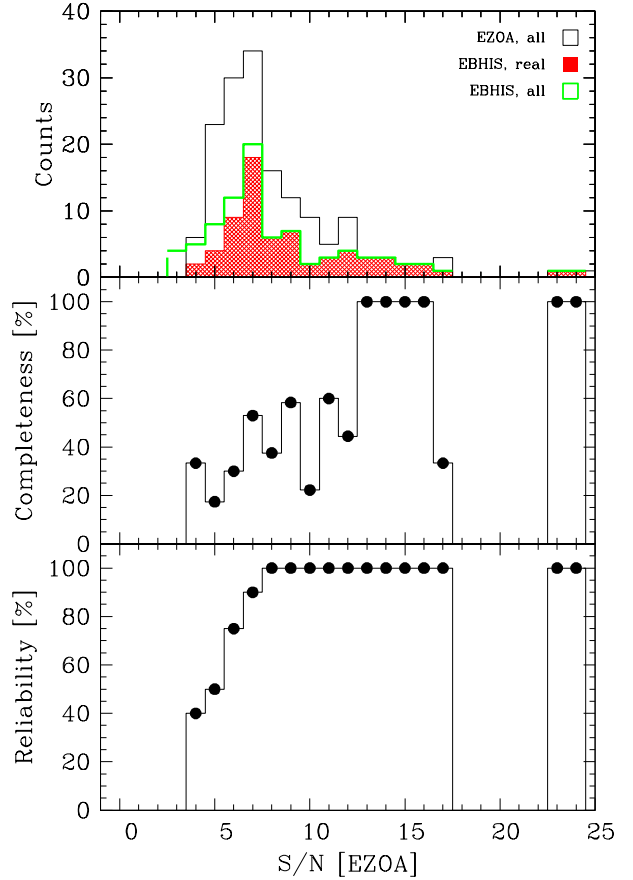


Figure A1. Top panel: Histogram of SNR of all EZOA detections (black), all EBHIS source candidates (thick green), and real EBHIS sources (hashed red). Middle panel: Completeness of the EBHIS shallow source catalogue as a function of SNR. Bottom panel: Reliability of the EBHIS sources as a function of SNR.

APPENDIX A: THE PRELIMINARY EBHIS SHALLOW SOURCE CATALOGUE

The EBHIS shallow source catalogue comprises 89 sources¹⁴ for $|b| \leq 6^\circ$. A comparison with our catalogue confirms 73 of these sources as real, the others are caused either by a combination of high noise peaks and baseline variation or are too faint for a decision. Among the EBHIS *candidates* (i.e., detections found by the automated source finder before being classified by the neural network algorithm; $N = 26,586$ for $|b| \leq 6^\circ$) are a further 48 real detections (0.2%).

Taking our EZOA catalogue as reference, the EBHIS shallow source catalogue is complete only for sources with a peak signal-to-noise ratio (SNR) > 13 but is reliable from SNR = 8 onwards, as shown in Fig. A1, middle and bottom panel, respectively. This is only an estimate, though, since the statistics are low, as shown in the top panel of Fig. A1.

The overall reliability of the EBHIS shallow source catalogue in the ZoA is 82%, improving to 98% for flux densities

¹⁴ One additional source with $b = 6^\circ 15'$ has also a cross-match in the EZOA catalogue (EZOA J0314+64) but since the detection goes beyond the edge of our (cut-out) data cube, the fitted parameters are uncertain and thus this detection is excluded from this analysis.

above 10 Jy km s^{-1} . The rather low reliability is likely due to the influence of the large number of continuum sources in the Galactic plane on the baselines (Staveley-Smith et al. 2016) and thus on the automated source finding and classification. In addition, the low number statistics combined with large uncertainties add a large error to the rates we have found.

Note that during the fine-tuning of the pipeline used for the compilation of the EBHIS shallow source catalogue, a comparison with our visual search was used to improve the neural network algorithm that discriminates between good and unreliable candidates. A comparison of this initial catalogue with the latter one confirms that, as intended, the latter catalogue is somewhat more reliable but less complete; this concerns mainly detections in the range $7 \lesssim \text{SNR} \lesssim 12$.

APPENDIX B: NOTES TO INDIVIDUAL EZO A GALAXIES

J1856–03: This source was detected as HIZO A J1855–03B by Staveley-Smith et al. (2016): There is a possible galaxy faintly visible in the NIR at (RA,Dec)=(18:56:00.5, –03:12:21) at a distance of $2'.2$ to the HI position. It is large and diffuse and, if real, matches the profile well.

J1929+08: Also detected as HIZO A J1929+08 by Donley et al. (2005); their profile shows a clearly confused profile while our (weaker) profile is rather noisy. The images show two galaxies of similar size and appearance, both listed in the Deep Sky Hunters catalogue by Kronberger et al. (2006). DSH J1929.3+0802 is also an IRAS source.

J1919+14: The HI detection is affected by a strong baseline variation which affects the fitted parameters. It was also detected by Donley et al. (2005) at a distance of $5'.2$ to our HI position. No obvious candidate could be found around either position but the extinction is very high at $A_K = 2^m6$.

J1921+14: This is an area of high extinction ($A_K = 1^m7$, variable across the search region) and star crowding. The UKIDSS images show a diffuse detection consistent with the HI parameters.

J2000+18: The flux determination may be affected by an RFI in the range $3900 - 4000 \text{ km s}^{-1}$ which was not completely removed during the reduction process.

J2001+26: There are three galaxies in the field, one of which (2MASX J20010969+2655338) was observed by Kraan-Korteweg et al. (2018) with the NRT but not detected. The other two galaxies are not listed in the literature: the galaxy at (RA,Dec)=(20:01:26.4,+26:59:40) is diffuse and matches the HI parameters well, while the galaxy at (RA,Dec)=(20:01:26.7,+26:55:36) at a larger distance of $3'.6$, is an early spiral and similar in appearance to 2MASX J20010969+2655338.

J2029+31: Despite being a high SNR detection (9.0), the distance between the fitted position and the counterpart is rather large ($d=3'.4$). However, the position fitted by SoFiA is much closer ($d=0'.5$), and the diffuse appearance of the galaxy agrees well with the HI parameters.

J2050+47: Though only faintly visible on UKIDSS images, the galaxy is confirmed on WISE images.

J2102+46: There are two galaxies in the area, neither of which is listed in the literature. The galaxy at (RA,Dec)=(21:02:33.9,+46:05:52), which is faintly visible with WISE,

appears to be larger and matches the HI parameters better than the galaxy at (RA,Dec)=(21:02:49.9,+46:09:05).

J2130+48: There are two large galaxies in the field: 2MASX J21305323+4813559 at $d=1'.5$ and 2MASX J21310014+4814279 at $d=1'.6$. Both were observed by Kraan-Korteweg et al. (2018) with the NRT which confirmed that 2MASX J21310014+4814279 is the counterpart. 2MASX J21305323+4813559 has also an optical velocity of 3556 km s^{-1} (Seeberger & Saurer 1998).

J2131+43: The images show six galaxies, four of which form a tight group (with possible interaction) at a rather large distance from our HI position, $d=3'.1$, and listed in the 2MASX catalogue as a single detection, 2MASX J21312321+4336182. It is also an IRAS source (IRAS 21295+4323) with an optical velocity of $v = 5467 \pm 56 \text{ km s}^{-1}$ (Strauss et al. 1992). There are two HI observations of this group (Paturel et al. 2003, Masters et al. 2014), both of which show our profile (5500–5750) as well as a low-velocity shoulder which can be seen in the EBHIS cube as a possible, fainter detection near-by and which is likely due to galaxies in this group. The cross-match to our detection is most likely an unlisted galaxy at (RA,Dec)=(21:31:17.9,+43:39:03) and $d=0'.4$. There is another, fainter galaxy visible at (RA,Dec)=(21:31:16.9,+43:38:01), $d=1'.4$, which may also belong to the group.

J2143+46: This HI detection is likely confused. There are two large galaxies in the field: UGC 11802 at $d=0'.5$ and UGC 11806 at $d=3'.1$. Both are IRAS sources and of similar size and morphological type, but UGC 11806 is more inclined. Optical velocities are $v = 3100 \pm 18 \text{ km s}^{-1}$ and $v = 3273 \pm 18 \text{ km s}^{-1}$ (Karachentsev 1980), respectively. Both have also been observed by Theureau et al. (1998) with the NRT and were detected at $v = 3153 \text{ km s}^{-1}$ and 3322 km s^{-1} , respectively.

J2237+53: There are two galaxies in the field, both of which contribute to the HI detection. Both are of similar size but 2MASX J22370662+5357049 ($d=0'.4$) is nearly edge on while 2MASX J22370933+5358339 ($d=1'.2$) is fairly inclined and detected with IRAS. The former was observed by Seeberger, Huchtmeier & Weinberger (1994) with the Effelsberg radio telescope with a similar profile to ours. The latter was observed by Courtois et al. (2009) and Paturel et al. (2003) with the Green Bank 300-foot telescope (GBT) and the NRT, respectively. The GBT profile in particular shows clearly two double horns with a low shoulder at $v < 5400 \text{ km s}^{-1}$ too faint to be visible in the EBHIS data.

J0020+59: This HI detection is the close-by dwarf IC10. The extinction at this position is overestimated since at latitudes $|b| < 5 \text{ deg}$ IRAS sources were not all removed from the DIRBE/IRAS extinction maps (Schlegel, Finkbeiner & Davis 1998) and this galaxy is infrared-bright. It is also resolved with respect to the telescope beam. More details are given in Sec. 7.1.1.

J0213+66: There are two galaxies of similar appearance in the field, one is slightly rounder than the other. The HI detection shows no indication of confusion, and it is not possible to decide which of the galaxies is the counterpart.

J0233+58: The HI detection shows a narrow single-peak profile; there is a galaxy pair in the field consisting of one larger, elongated galaxy and one smaller, roundish companion. The extinction is $A_K = 0^m3$ and no deep NIR images are available, hence it is not possible to decide if one of the

galaxies is nearly face-on. The larger galaxy was detected by IRAS and is thus more likely to be the counterpart.

J0243+59: This detection is Maffei 2 and heavily affected by Galactic H I contamination. The position and H I parameters are unreliable. The position as determined by SoFIA, (RA,Dec) = (02:42:03.3,+59:37:25), is much closer to the galaxy's position ($d = 1'.5$).

J0252+62: The distance between the H I position and the counterpart ($d = 4'.0$) is larger than could be expected for an SNR of 9.3. An inspection of the cube shows a possible contamination at lower Galactic latitude which may be a possible detection of a very LSB galaxy at (RA,Dec) = (02:51:53.2,+62:27:43) and $d = 4'.4$.

J0253+55: Outside the nominal search radius is a prominent galaxy pair: 2MASX J02531475+5528143 at $d = 4'.3$ and 2MASX J02531969+5529140 at $d = 4'.6$. Paturel et al. (2003) have observed the former while Kraan-Korteweg et al. (2018) have observed the latter, both with the NRT and showing similar profiles, but only measuring half the flux of our detection. The galaxy pair can therefore be ruled out as the counterpart. Instead, at $d = 2'.1$ an unpublished LSB is visible which matches the H I parameters well.

J0255+57: The DSS images show a very faint detection at (RA,Dec) = (02:55:16.9,+56:59:24) which is confirmed on the WISE images; there are no deep NIR images.

J0308+62: The counterpart is only faintly visible on DSS and WISE images; there are no deep NIR images.

J0314+64: This H I detection is located at the edge of the cube and position and H I parameters are uncertain.

J0332+58: The detection is a close-by dwarf galaxy ($v = 1430 \text{ km s}^{-1}$, $\log(M_{\text{HI}}) = 8.7$). The UKIDSS images show a large, diffuse emission at (RA,Dec) = (03:32:48.4,+58:14:55) which, if confirmed, is the counterpart.

J0345+49: Though the distance of $4'.5$ between the H I position and the counterpart is rather large for an SNR of 7.4, at the low extinction of $A_K = 0^m.3$ and the large H I mass of $\log(M_{\text{HI}}) = 9.8$ we can expect to see the counterpart, and 2MASX J03455024+4914144 matches the H I parameters well.

J0437+54: There are two bright galaxies within the search radius: 2MASX J04373506+5414339 at $d = 1'.5$ seems to be little inclined, while 2MASX J04374087+5415389 at $d = 2'.7$ is highly inclined; optical redshifts are $v_{\text{opt}} = 5369 \text{ km s}^{-1}$ and $v_{\text{opt}} = 5653 \text{ km s}^{-1}$ (Huchra et al. 2012), respectively, compared to our $v_{\text{hel}} = 5341 \text{ km s}^{-1}$. The latter galaxy was observed by Paturel et al. (2003) with the NRT at $v = 5356 \text{ km s}^{-1}$, but judging by the optical redshifts it is likely they detected 2MASX J04373506+5414339 instead which lies well in the NRT beam.

J0437+43: Two large galaxies are visible within the search radius. The galaxy at $d = 1'.4$ is UGC 03098 with an optical redshift of $v_{\text{opt}} = 4287 \pm 150 \text{ km s}^{-1}$ (Hill et al. 1988), while the companion, 2MASX J04370607+4355349 at $d = 0'.8$, is an IRAS detection and appears disturbed. UGC 03098 was detected by Springob et al. (2005) with the GBT and by Staveley-Smith & Davies (1987) with PKS. Both show a lopsided profile similar to ours which may be confused. It is not possible to tell which galaxy contributes how much to the profile.

J0438+44: UGC 03108, at $d = 4'.4$ from the H I position, was observed by Springob et al. (2005) with the GBT and

detected at $v = 3959 \text{ km s}^{-1}$. Their profile is wider than ours and shows our profile as a lopsided high-velocity horn. We do not see the wider profile in our data due to the lower sensitivity of the EBHIS survey.

J0440+49A and J0440+49B: There are two barely separated H I detections visible in the H I cube: the profile of J0440+49B covers $3750 - 3980 \text{ km s}^{-1}$ and has a reliable W_{50} , while J0440+49A starts at $v \simeq 3600 \text{ km s}^{-1}$ and goes also up to $v \simeq 3980 \text{ km s}^{-1}$. Its w_{20} is close to the full line width of this galaxy (bar the fact that the peak is dominated by the J0440+49B profile). The images show a galaxy pair with one strongly inclined (broad line width) and the other nearly face-on (narrow line width).

J0446+44: Though there are many galaxies visible on the UKIDSS images, all seem too small for a velocity of 6434 km s^{-1} and H I mass of $\log(M_{\text{HI}}) = 9.8$. They are all likely part of a cluster at higher redshift.

J0455+34: The cross-match looks asymmetric and disturbed which makes it difficult to estimate whether the galaxy could lie at a redshift of $v = 3256 \text{ km s}^{-1}$.

J0506+31: The cross-match is faint and diffuse, located near the edge of the UKIDSS image. WISE images confirm this to be a galaxy. Another WISE galaxy, WISEP J050601.69+314037.8 at $d = 1'.3$, is likely further away (Rebull et al. 2011).

J0520+43: There are two large galaxies in the field, possibly a pair. Our cross-match, 2MASX J05200866+4314313, is an early type galaxy while the other galaxy (2MASX J05201415+4318214 at $d = 3'.2$) is a medium type spiral. The former galaxy was detected with a similar profile by Kraan-Korteweg et al. (2018), while the latter was observed by Takata et al. (1994) with different H I parameters.

J0546+31: One large galaxy and at least four smaller ones are visible on the images, possibly a galaxy group. The largest is the most likely counterpart.

J0554+18: The images show two large early-type galaxies and several smaller ones, possibly part of a galaxy group. The most likely counterpart is 2MASX J05540715+1759352, a face-on early-type spiral which shows strong star formation on WISE images.

J0607+16: Well inside the search area lies a galaxy pair: 2MASX J06074379+1608036 at $d = 1'.4$ (inclined, barred spiral) and 2MASX J06074754+1604526 at $d = 2'.0$ (edge-on spiral). The former was detected by Kraan-Korteweg et al. (2018) with the NRT as clearly confused (and more lopsided than our profile). 2MASX J06074754+1604526 was observed with Parkes by Said (priv. comm.) which shows steeper edges and a pronounced peak at $v \simeq 5600 \text{ km s}^{-1}$ as opposed to the NRT profile, indicating that both galaxies contribute to our profile.

J0620+20: Two diffuse galaxies can be seen within the search radius; both were detected in the Arecibo Dual Beam Survey (ADBS, Rosenberg & Schneider 2000) at $v = 1320 \text{ km s}^{-1}$ (same as our detection) and at $v = 2272 \text{ km s}^{-1}$ (too faint to be detected by us), respectively.

J0649+09: This galaxy was also detected by Donley et al. (2005) with PKS. The most likely cross-match is 2MASX J06493148+0939437 at $d = 3'.3$. A very diffuse late-type galaxy that is closer to the H I position ($d = 0'.3$) is less likely but cannot be excluded as counterpart; it is possible that it contributes to the profile (not obvious, though) and thus explains the larger distance to 2MASX J06493148+0939437.

J0636+00: There is a close galaxy pair in the field: 2MASX J06362668+0055433 is an inclined spiral (with a possible small companion to the north) while 2MASX J06362361+0055513 appears more face-on. The profile does not show an indication of confusion (though it cannot be excluded), and the inclined spiral, which is also an IRAS source, seems to be the more likely counterpart.

J0700–04: Begum et al. (2005) observed this galaxy with the VLA and found that the HI emission comes from two dwarf galaxies. Both are faintly visible on the deep NIR images. See Sec. 7.1.2 for more details.

This paper has been typeset from a $\text{\TeX}/\text{\LaTeX}$ file prepared by the author.